Nested Large-Eddy Simulations of the Intermittently Turbulent Stable Atmospheric Boundary Layer over Real Terrain

BOWEN ZHOU AND FOTINI KATOPODES CHOW

Civil and Environmental Engineering, University of California, Berkeley, Berkeley, California

ABSTRACT

The nighttime stable atmospheric boundary layer over real terrain is modeled with nested high-resolution large-eddy simulations (LESs). The field site is located near Leon, Kansas, where the 1999 Cooperative Atmosphere–Surface Exchange Study took place. The terrain is mostly flat with an average slope of 0.5°. The main topographic feature is a shallow valley oriented in the east–west direction. The night of 5 October is selected to study intermittent turbulence under prevailing quiescent conditions. Brief turbulent periods triggered by shear-instability waves are modeled with good magnitude and temporal precision with a dynamic reconstruction turbulence closure. In comparison, conventional closures fail to excite turbulent motions and predict a false laminar flow. A plausible new intermittency mechanism, previously unknown owing to limited spatial coverage of field instruments at this site, is unveiled with the LESs. Turbulence can be generated through gravity wave breaking over a stagnant cold-air bubble in the valley upwind of the main tower. The bubble is preceded by the formation of a valley cold-air pool due to down-valley drainage flows during the evening transition. The bubble grows in depth by entraining cold down-valley and downslope flows from below and is eroded by shear-induced wave breaking on the top. The cyclic process of formation and erosion is repeated during the night, leading to sporadic turbulent bursting.

1. Introduction

After sunset, the atmospheric boundary layer becomes stably stratified owing to outgoing longwave surface radiation. The intensity of turbulence in the stable boundary layer (SBL) is determined by the competing forcings of shear and buoyancy. Depending on their relative strength, the SBL falls into the continuously turbulent regime dominated by shear production, the quiescent regime dominated by buoyancy destruction, or the intermittent regime where both forcings are important (Stull 1988).

Global intermittency in the atmosphere is characterized by buoyancy-suppressed turbulence over prolonged periods greater than the time scale of the dominant eddies and energetic mixing events, known as turbulent bursts, occurring over relatively short periods (Nakamura and Mahrt 2005). Turbulence in the SBL is often intermittent especially on clear nights with weak winds.

Strong stratification results from radiative cooling and low wind shear, hence limiting upward mechanical mixing. This is referred to as boundary-layer decoupling over cold surfaces (Derbyshire 1999). Under these circumstances, sporadic bursts of turbulence can recouple the surface layer with the atmosphere above. These bursts are responsible for the majority of the upward transport of heat and downward transport of momentum.

During the 1999 Cooperative Atmosphere–Surface Exchange Study (CASES-99) (Poulos et al. 2002), shear-instability waves were observed for a brief period of approximately 30 min on the night of 5 October (Blumen et al. 2001). A lidar scan presented in Fig. 1 reveals the horizontal structure of the billows. They were observed at an elevation of about 40 m above ground level (AGL), with a wavelength of about 350 m. They propagated with a phase speed of $5.25\,\mathrm{m\,s^{-1}}$ to the north. Newsom and Banta (2003, hereafter NB03) associated an inflection point in the mean wind profile with the onset of the billows. They pointed out that the increase in vertical shear was due to a slowing down of the flow from below. The cause of this flow retardation remained an open question owing to the limited spatial coverage of field equipment.

Corresponding author address: Tina Chow, Department of Civil and Environmental Engineering, 621 Davis Hall, University of California, Berkeley, Berkeley, CA 94720-1710.
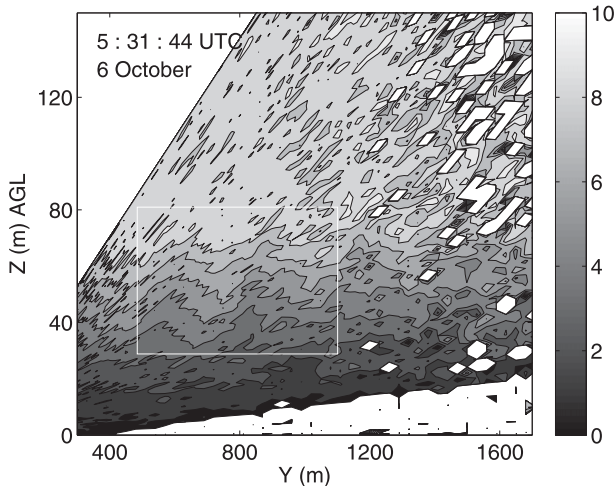E-mail: tinakc@berkeley.edu

FIG. 1. Vertical slice scan of radial velocity measured by HRDL at 0531 UTC 6 Oct. Wave patterns between 30 and 60 m AGL are indicated by the white box. Positive radial velocities indicate flow away from the HRDL; white spots are due to missing data. Contour interval is $1\,m\,s^{-1}$.

Motivated by this puzzle, this paper sets out to investigate this event, in the hope of advancing the understanding of intermittency from wave-generated turbulence. With a numerical modeling approach, we attempt to reconstruct a complete 3D history of the formation, evolution, and breaking of the shear-instability waves.

2. General description of IOP2 during CASES-99

CASES-99 was conducted over the Great Plains of the United States near Leon, Kansas, from 1 to 31 October 1999. The local terrain is relatively flat (average slope is 0.5°), has mostly homogeneous land cover (prairie grass), and lacks obstacles. This study focuses on the night of 5 October in local standard time (LST) or 6 October in coordinated universal time (UTC) during the second intensive observation period (IOP2). It was a clear night with relatively calm conditions. A low-level jet was observed with peak wind speeds around $10\,m\,s^{-1}$ at approximately 110 m AGL. A temperature inversion

of 8 K over the lowest 80 m was established early in the night. Some time-averaged point measurements are presented in Table 1. According to the SBL classification by Van de Wiel et al. (2003), which is based on large-scale pressure gradients and net surface radiation, 5 October is an intermittently turbulent night. Compared to a continuously turbulent night (e.g., 6 October) differences in turbulent statistics are vast. For example, the 6-h-averaged friction velocity is nearly 6 times smaller on 5 October.

The sporadic nature of turbulence is also apparent from time series of thermocouple temperature measurements at the 60-m main tower in Fig. 2. The amplitude of temperature fluctuations was much smaller during IOP2 than the following night. A surface inversion is present, as represented by an increase in temperature with height. In comparison, the surface layer was well mixed on 6 October, where temperature measurements at different heights are indistinguishable (see embedded plot in Fig. 2).

A period with rapid temperature fluctuations between 0500 and 0600 UTC (0000–0100 LST) 6 October stands out in Fig. 2. The elevated turbulence was triggered by shear-instability waves between 30 and 60 m AGL, as seen from the high-resolution Doppler lidar (HRDL) presented in Fig. 1 (see also Fig. 1 of NB03). The HRDL was located 1.45 km south of the main tower and performed shallow vertical scans at an azimuth of 10° pointing toward north. A detailed observational analysis leading to the conclusion that the observed patterns in Fig. 1 are shear-instability waves is given in NB03. Recently, Sun et al. (2012) analyzed intermittent turbulence during the CASES-99 campaign, and classified this event as a category C turbulence intermittency (see their section 4c and Fig. 15). This category is characterized by a moderate turbulence regime, when top-down turbulence sporadically burst into the otherwise weak turbulence regime.

3. Model configuration and description

The Advanced Regional Prediction System (ARPS) is used for the simulations. ARPS is developed at the

TABLE 1. Basic meteorological variables during the night of 5–6 and 6–7 Oct: U_{10m} and T_{10m} are the wind speed and temperature, respectively, at 10 m AGL, T_s is the surface temperature, Z_i is the depth, u^* is the friction velocity, H is the sensible heat flux, and Q_{net} is the net radiation budget of the surface. Values are from Van de Wiel et al. (2003).

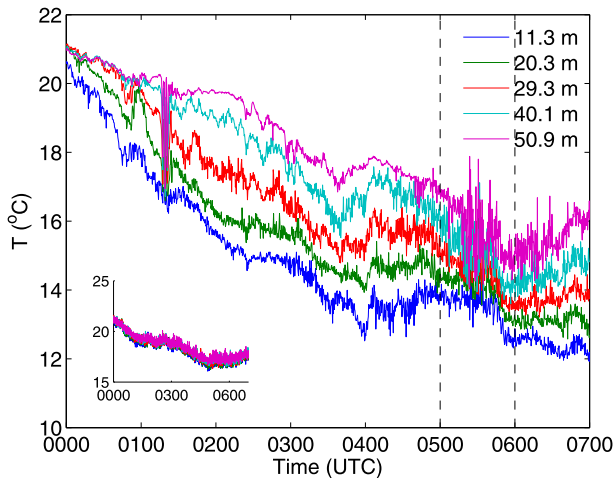| Date	Time (LST)	U_{10m} ($m\,s^{-1}$)	T_{10m} (K)	T_s (K)	Z_i (m)	u^* ($m\,s^{-1}$)	H ($W\,m^{-2}$)	Q_{net} ($W\,m^{-2}$)	Class
6 Oct	0000–0600	2.82	285.16	281.41	75	0.075	−6.9	−61.7	Intermittently turbulent
7 Oct	0000–0600	6.40	288.80	286.57	145	0.438	−48.4	−71.2	Continuously turbulent

FIG. 2. Time series of thermocouple temperature on 5–6 and 6–7 Oct (embedded plot). Data are taken at 11.3, 20.3, 29.3, 40.1, and 50.9 m AGL (see legend) and resampled at every 20 s. The turbulent episode is enclosed by dashed lines.

Center for Analysis and Prediction of Storms at the University of Oklahoma. It is a nonhydrostatic mesoscale and small-scale finite difference model. ARPS uses a terrain-following coordinate system on an Arakawa C grid. A mode-splitting time integration scheme is employed (Klemp and Wilhelmson 1978). This technique divides a big integration step Δt_{big} into a number of computationally inexpensive small time steps Δt_{small} to update the acoustically active terms, while all other terms are computed once every big time step. A thorough description of the model can be found in Xue et al. (2000, 2001), with relevant details presented below.

a. One-way nested configuration

ARPS has a one-way grid nesting capability; that is, the lateral boundary conditions of a smaller inner domain are obtained from a larger outer domain. The largest domain usually obtains its initial and lateral boundary conditions from reanalysis data. In this study, a total of four nest domains are adopted (see Table 2). Simulations are initialized with the North American Regional Reanalysis (NARR) at 32-km horizontal resolution, and one-way nested down to a fine grid with 25-m horizontal and 10-m vertical spacing (see Fig. 3). The average vertical resolution ranges from 300 m for the outermost domain to 10 m for the innermost domain. Grid stretching is applied in the vertical direction. On the innermost domain, the near-surface vertical spacing is 2 m, and the first 200 m above the surface is represented by 70 grid points. The size of the innermost domain is 9 km × 9 km × 1.2 km, represented by (360, 360, 120) grid points. The nesting ratio, which is the ratio of horizontal domain length of two adjacent nests, is 5-to-1[1] in this study, except for the finest nest. All domains are centered at the main tower location (35.6485°N, 96.7361°W), also with the exception of the innermost domain. It is nested with an approximately 3-to-1 ratio, and centered at (37.64°N, 96.7361°W), to include an important topographic feature (i.e., a shallow valley to the south of the main tower).

For all domains, the inner nest obtains lateral boundary conditions from the outer nest at a constant time interval ΔT_b. It does so by first checking out two adjacent snapshots in time separated by ΔT_b from the outer nest, and then linearly interpolates these two snapshots in time to provide itself with lateral boundary conditions at every time step. Michioka and Chow (2008) demonstrated the importance of frequent boundary updates for inner domains. We followed a similar setup, using smaller ΔT_b with the decreasing domain sizes. For the smallest domain, the lateral boundaries are updated every 180 s. A relaxation zone of the Davies (1983) type is used to control numerical wave reflections. On the bottom boundary, high-resolution ⅓ arc-s (~10 m) topography from the U.S. Geological Survey (USGS) National Elevation Dataset and land cover at 30-m resolution from the National Land Cover Database 2006 are used to represent the real terrain from the 640-m grid onward. ARPS downsamples the topography and land cover onto the numerical grid, and applies a smoothing filter to remove small-scale noises introduced in this procedure. The finest terrain contour is plotted in Fig. 3. A Rayleigh damping layer is set for roughly one-third of the domain height (see Table 2) from the top.

b. Turbulence model

Following the recommendation of Xue et al. (1996), the boundary layer parameterization of Sun and Chang (1986) is used for the mesoscale grids at 6400-m spacing. The 1.5-order turbulent kinetic energy-based closure (TKE-1.5) of Moeng (1984) is used on all computational domains with grid size smaller than 6400 m. In addition, an explicit filtering and reconstruction large-eddy simulation (LES) approach with the dynamic Wong and Lilly model (DWL) (Wong and Lilly 1994) and the reconstruction model (Chow et al. 2005) are used on the 25-m LES grid to investigate model sensitivity to the turbulence closure.

---

[1] The domain size ratio between nests 1 and 2 is 5.2 owing to a switch in computational cluster.

TABLE 2. List of nested simulation parameters: Δx, Δy, and Δz are the average horizontal and vertical spacings, Δz_{min} is the vertical spacing near the surface, ΔT_b is the lateral-boundary update interval, and Δt_{big} and Δt_{small} are the large and acoustic time steps.

Nest	No. of grid points (nx, ny, nz)	Domain (km)	$\Delta x/\Delta y$ (m)	$\Delta z/\Delta z_{min}$ (m)	ΔT_b (s)	Δt_{big} (s)	Δt_{small} (s)	Grid levels below 200 m
1	(100, 100, 60)	$640 \times 640 \times 18$	6400	300/50	10 800	5.0	5.0	5
2	(192, 192, 100)	$123 \times 123 \times 10$	640	100/20	1800	1.0	1.0	11
3	(192, 192, 100)	$24.6 \times 24.6 \times 2$	128	20/4	900	0.5	0.1	27
4	(360, 360, 120)	$9 \times 9 \times 1.2$	25	10/2	180	0.025	0.025	70

As previous studies have shown (Chow et al. 2005; Chow and Street 2009; Zhou and Chow 2011), explicit filtering and reconstruction greatly improves the subfilter-scale (SFS) representation of turbulence on both flat and complex terrain. The reconstruction procedure is based on explicit filtering of the Navier–Stokes equations:

$$\frac{\partial \overline{\tilde{\rho}\tilde{u}_i}}{\partial t} + \frac{\partial \overline{\tilde{\rho}\tilde{u}_i\tilde{u}_j}}{\partial x_j} = -\frac{\partial \overline{\tilde{p}}}{\partial x_i} - \overline{\tilde{\rho}}g\delta_{i3} + \overline{\tilde{\rho}}\epsilon_{imn}f_n\overline{\tilde{u}}_m - \frac{\partial \overline{\tilde{\rho}\tilde{\tau}_{ij}}}{\partial x_j}, \quad (1)$$

$$\frac{\partial \overline{\tilde{\rho}}}{\partial t} + \frac{\partial \overline{\tilde{\rho}\tilde{u}_i}}{\partial x_i} = 0, \quad (2)$$

$$\frac{\partial \overline{\tilde{\theta}}}{\partial t} + \frac{\partial \overline{\tilde{\rho}\tilde{u}_i\tilde{\theta}}}{\partial x_i} = -\frac{\partial \overline{\tilde{\rho}\tilde{\chi}_i}}{\partial x_i}, \quad (3)$$

where the explicit filter is denoted by an overbar and the implicit discretization operators denoted by a tilde $\overline{\tilde{u}}_i$ are the velocity components, $\overline{\tilde{p}}$ is the pressure, $\overline{\tilde{\rho}}$ is the density, f is the Coriolis parameter, and $\overline{\tilde{\theta}}$ is the potential temperature. We assume all filtering is with a Favre-type density-weighted filter (details in Chow 2004). The moisture transport equation is similar to the potential temperature equation and is not presented here.

Traditionally, the discretization procedure is treated as an implicit filter based on the finite difference–volume methods. Implicit filtering can lead to truncation and aliasing errors in the nonlinear terms (Lund 1997). Explicit filtering can minimize the influence of truncation errors and has been shown to be beneficial in LES (Lund 1997; Gullbrand 2001; Carati et al. 2001; Winckelmans et al. 2001; Gullbrand and Chow 2003). In this study, a top-hat filter of width twice the grid spacing is applied. With the explicit filtering procedure, turbulent momentum and heat fluxes can be decomposed into resolvable subfilter-scale (RSFS) and subgrid-scale (SGS) stresses:

$$\tau_{ij} = \overline{u_i u_j} - \overline{u}_i\overline{u}_j = \underbrace{(\overline{u_i u_j} - \overline{\tilde{u}_i\tilde{u}_j})}_{\tau_{SGS}} + \underbrace{(\overline{\tilde{u}_i\tilde{u}_j} - \overline{u}_i\overline{u}_j)}_{\tau_{RSFS}}, \quad (4)$$

$$\chi_i = \overline{u_i\theta} - \overline{u}_i\overline{\theta} = \underbrace{(\overline{u_i\theta} - \overline{\tilde{u}_i\tilde{\theta}})}_{\chi_{SGS}} + \underbrace{(\overline{\tilde{u}_i\tilde{\theta}} - \overline{u}_i\overline{\theta})}_{\chi_{RSFS}}. \quad (5)$$

The SGS stresses are of scales finer than the grid resolution and must be modeled. The RSFS stresses depend on the resolved and explicitly filtered fields and can be restored based on knowledge of the explicit filter. The unfiltered velocity is obtained through the approximate deconvolution method (ADM) of van Cittert (1931) and Stolz et al. (2001):

$$\tilde{u}_i = \overline{\tilde{u}}_i + (I - G) * \overline{\tilde{u}}_i + (I - G) * [(I - G) * \overline{\tilde{u}}_i] + \cdots, \quad (6)$$

where I is the identity operator, G is the explicit filter, and the asterisk is the convolution operator. The number of terms on the right-hand side is referred to as levels of reconstruction. A truncated series of the above equation is used to approximate $\tilde{u}_i$. For example, with one level reconstruction (abbreviated as ADM0) $\tilde{u}_i \approx \tilde{u}_i^\star = \overline{\tilde{u}}_i + (I - G) * \overline{\tilde{u}}_i$, and $\tilde{u}_i^\star$ is used in the RSFS terms. The
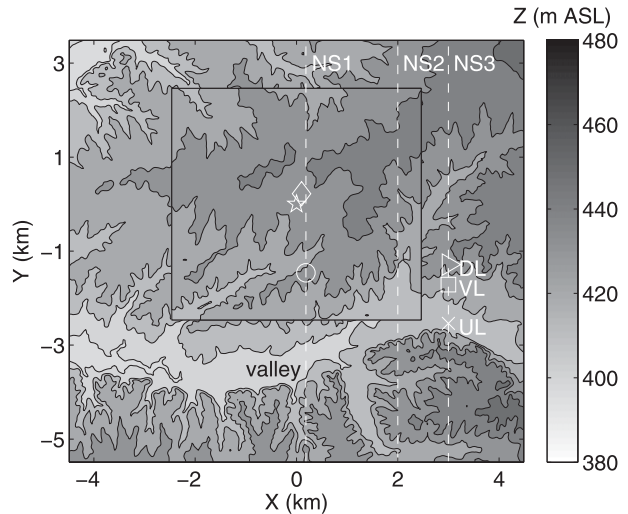

FIG. 3. Elevation contours of the two 25-m LES domains, with the smaller one enclosed by solid lines. Location of the tower is marked by a star, the radiosonde is marked by a diamond, and the lidar is marked by a circle. The dashed line represents three north–south slice locations (NS1, NS2, and NS3). Three sites along NS3 are marked by a cross, a square, and a triangle for the upwind, valley, and downwind location, respectively. Contour interval is 10 m.

TABLE 3. List of nested simulation parameters on the 25-m LES grid. The "initial condition" column refers to runs presented in Table 2; T_{start} is the starting time of the simulation. In the "run name" column, "-S" is short for small domain and "-R" is short for restart run.

Run name	Lateral grid size	Initial condition	SGS closure	RSFS closure (Rec-level)	T_{start}
TKE	360	Nest 3	TKE-1.5	—	2100 UTC 5 Oct
DWL–ADM0	360	Nest 3	DWL	0	2100 UTC 5 Oct
TKE-S	192	Nest 3	TKE-1.5	—	2100 UTC 5 Oct
TKE–ADM1-R	360	Nest 4	TKE-1.5	1	0400 UTC 6 Oct
DWL-R	360	Nest 4	DWL	—	0400 UTC 6 Oct
DWL–ADM0-R	360	Nest 4	DWL	0	0400 UTC 6 Oct

RSFS model can be combined with most eddy-viscosity closures (e.g., TKE–ADM) to improve model performance under the explicit filtering framework. When used with a dynamic SGS closure (e.g., DWL–ADM) the overall SFS representation is called the dynamic reconstruction model (DRM).

The RSFS–SGS model framework can be viewed as a mixed model (Bardina et al. 1983; Zang et al. 1993). The RSFS component is the so-called scale-similarity term represented by reconstruction, and the SGS component is represented with an eddy-viscosity model. The original scale-similarity model of Bardina et al. (1983) assumed that the smallest resolved scales have a similar structure to the subfilter scales. The reconstruction model seeks a more accurate representation of the resolved scales by inverting the explicit filter operation. With higher levels of reconstruction, model details of high-frequency motions approaching the filter cutoff are restored, thus improving the representation of the SFS stresses. In addition, the RSFS formulation term allows backscatter of energy from SFS to resolved scales. This is especially important for the transition from quiescent to turbulent flows in the SBL (Zhou and Chow 2011).

Finally, important details of the model setup are given in Table 2. We simulate 10 h of the SBL starting from late afternoon [2100 UTC (1600 LST) 5 October] to past midnight [0700 UTC (0200 LST) 6 October]. A total of six LES runs are performed on the finest 25-m grid; see Table 3. Those include three 10-h full runs initialized from the 128-m grid and three partial runs for sensitivity studies. These three partial runs are initialized with the 3D field from nest 4 (see Table 2) at 0400 UTC 6 October and carried out for 3 h. Additional model parameters for the LES runs are listed in Table 3, which will be further explained in sections 4b and 4c.

4. Model evaluation

In this section, model results are validated with field measurements. Sensitivity to three key model parameters—grid resolution, turbulence closure, and nest domain—are evaluated. In the process, we describe some key flow features during IOP2. From this point on, model data from the 25-m grid refers to the run with DWL–ADM0 (see Table 3, second row) as turbulence closure, except for section 4b, where model sensitivity to turbulence closure is explored.

a. Sensitivity to grid resolution

Figure 4 presents the vertical profiles of modeled wind speed U, wind direction ϕ, potential temperature θ, and specific humidity q at different grid resolutions. A log-scale y axis is used to stretch the surface layer. Radiosonde data at 0500 UTC is scarce within the SBL. Better-quality measurements obtained from the tower are presented in Fig. 5 and will be discussed below. Model results are in general agreement with measurements. Significant improvements in the lowest few hundred meters are achieved starting with the second nest level (the 640-m grid). The vertical profiles on the 128-m grid (the third nest) are similar to those on the 640-m grid. The 25-m grid results show improvements in the surface layer—mostly below 50 m AGL. For example, at 0259 UTC, near-surface wind speed is reduced by nearly $2 \, m \, s^{-1}$ from the 128- to the 25-m grid (the fourth and the finest nest), better matching the observed values.

Potential temperature is underpredicted by about 1 K below the daytime inversion layer (~700 m AGL) at 0000 UTC. Specific humidity is slightly overpredicted. This error is due to initial and lateral boundary conditions from NARR. It is likely caused by errors in the partitioning of sensible and latent heat fluxes. The under-/overestimation persists in the residual layer (RL) above the SBL throughout the simulation until 0500 UTC. In the boundary layer, modeled θ is up to 2 K warmer below 50 m AGL, except at 0500 UTC, when the modeled surface temperature agrees with the observations. Steeneveld et al. (2008) reported similar model overprediction of θ during strongly cooled nights. They proposed an alternative land surface scheme to overcome such error by introducing a vegetation layer. In this study, we used the ARPS default two-layer soil model (Noilhan
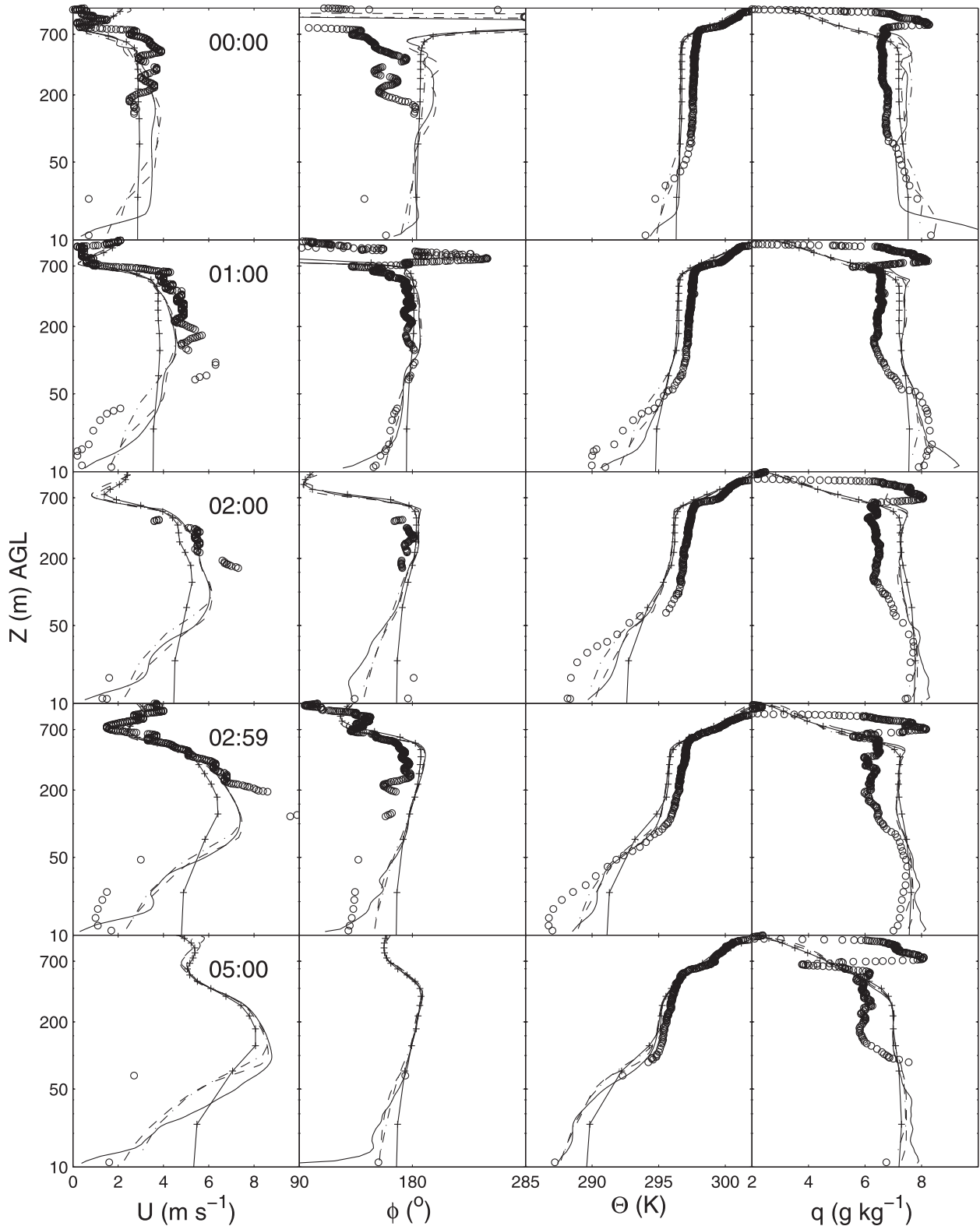
FIG. 4. Radiosonde observations (circles) compared with 6400- (solid line with plus signs), 640- (dashed–dotted line), 128- (dashed line), and 25-m (DWL–ADM0, solid line) simulations at the Leon GPS Loran Atmospheric Sounding System (GLASS) High-Resolution Sounding site (37.6510°N, 96.7350°W) for wind speed, wind direction, potential temperature, and specific humidity. The 6400-, 640-, and 128-m simulations are performed with TKE-1.5 as turbulence closure. (left) Sounding launch times (UTC) are given.
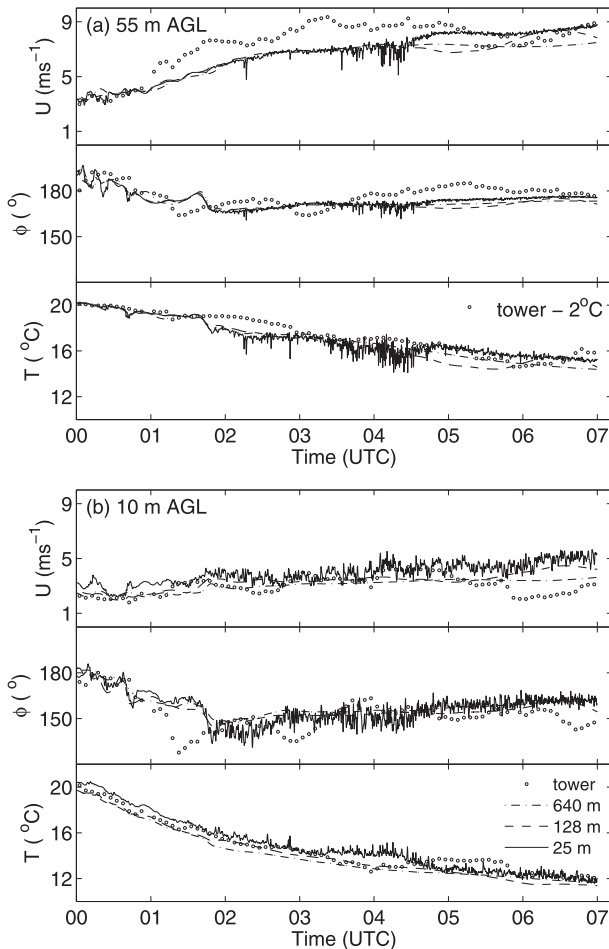
FIG. 5. Main tower observations compared with simulations at (a) 55 and (b) 10 m AGL for wind speed, wind direction, and temperature. Observed temperature at 55 m is subtracted by 2°C for comparison. Measurements are sampled every 5 min and model data every 2 s. The 640- and 128-m runs are performed with the TKE-1.5 closure and the 25-m run with the DWL–ADM0 closure.

and Planton 1989), and did not explore model sensitivity to land surface schemes. The warmer modeled temperature can also be caused by overmixing of potentially warmer air from above. However, this error does not seem to affect the dynamics of the observed bursting event at 0500–0600 UTC. By 0500 UTC, the model has caught up with the observed near-surface temperature (see bottom panel in Fig. 4). Instrument error is another possibility. As will be discussed below, the model temperature at 50 m AGL is colder than tower measurements. Therefore, there exists up to 4-K difference between the tower and the radiosonde measurements. Since the sounding site is merely 300 m north of the main tower (Poulos et al. 2002), we do not expect large horizontal temperature gradients within such small distances. According to Lundquist (2000), tower data are more reliable

than radiosondes in the surface layer during the CASES-99 field campaign.

A low-level jet (LLJ) develops near 110 m AGL around 0100 UTC. While the jet nose reaches $10 \, \text{m s}^{-1}$ at 0259 UTC according to radiosonde records, it is underpredicted by $2 \, \text{m s}^{-1}$ in the simulations. The maximum speed of the jet is determined by geostrophic pressure gradients. The underprediction of the jet speed is likely attributable to errors in the NARR data, because it is found on all grid levels. Near the surface, the modeled wind speeds are larger than Radiosonde observations. This could be due to overmixing in the model, which is also the likely cause of the warmer surface temperature as discussed above. Wind directions veer (turn clockwise) with height as a result of the Coriolis force. The angle between the geostrophic wind above the SBL and the surface wind is around 40° at 0259 UTC. This large angle is expected for a strongly stable ABL (Van Ulden and Holtslag 1985). The turning is well modeled by the 25-m simulation.

Time series of modeled wind speed, wind direction, and temperature are compared with the main tower observations, at tower top (55 m) and near the surface (10 m) in Fig. 5. With model data output every 2 s, only the 25-m run shows fluctuations in the series. Good agreement with the surface flow is achieved on all three inner domains (Fig. 5a). At the tower top, wind speed is underpredicted up to about $3 \, \text{m s}^{-1}$ from 0100 UTC onward, until 0500 UTC when the 25-m grid wind accelerates to the observed value of about $8 \, \text{m s}^{-1}$. Model temperature at 55 m is consistently colder than observations. This is in contrast to the comparison with the nearby radiosonde observation (see Fig. 4) where the model temperature is warmer. Better agreement is reached when the observed temperature is offset by 2°C in Fig. 5.

b. Sensitivity to turbulence closures

The SBL flow transitions into a turbulent period after 0500 UTC as shown in Fig. 2. A time–height contour plot of thermocouple temperatures at the main tower is presented in Fig. 6. LES with the TKE-1.5 closure (Fig. 6b) reproduces the mean profiles of temperature but fails to generate any turbulent fluctuations. To study model sensitivity to turbulence closures, three additional runs (TKE–ADM1-R, DWL-R, and DWL–ADM0-R) on the 25-m grid are performed (see last three rows of Table 3). These runs are restarted, hence the suffix "-R," from the TKE-1.5 run at 0400 UTC and integrated to 0700 UTC 6 October to save computational time. The purpose of these three runs is to determine whether the model can transition from a laminar to a turbulent state by improving the turbulence closure alone. The DWL-R run (Fig. 6c)

reveals strong temperature perturbations that resemble tower measurements. With the addition of a zero-level reconstruction term, the DWL–ADM0-R run (Fig. 6d) further improves the DWL results, and produces even stronger turbulent fluctuations. In comparison, the TKE–ADM1-R run does not show much improvement over the TKE results, hence it is not shown here. Because of computational resource limits, higher levels of reconstruction were not tested.

The normalized temperature variance spectra from the models are compared with thermocouple measurements in Fig. 7. Spectra are computed using Matlab's pwelch function (Welch 1967) during 0515–0542 UTC when the observed turbulent fluctuations are significant. The thermocouple spectrum peak at approximately 0.017 Hz corresponds to the dominant shear-instability wave frequency (see also Fig. 5 in NB03). The DWL–ADM0-R spectrum has a single sharp peak with lower frequency and higher amplitude than the observed peaks, while the DWL-R has a flatter top. Comparison of the DWL-R and DWL–ADM0-R reveals their difference in the partitioning of turbulent energy. The spectrum transitions from a broad flat shape (DWL-R) to a narrow sharp one (DWL–ADM0-R), suggesting that turbulent energy is partitioned toward high-frequency motions with the addition of the reconstruction model, better matching observations.

The above sensitivity study suggests that the DWL–ADM0 closure not only enables flow transition from quiescent to turbulent state, but also produces good results that match observations. Therefore, we repeated the entire 10-h simulation on the 25-m grid with the DWL–ADM0 closure. The time–height contour of temperature (Fig. 6e) reveals intense fluctuations similar to that of the DWL–ADM0-R run. The differences are due to the initial conditions. The temperature spectrum in Fig. 7 better matches the observed peak frequency and amplitude. However, it shows an additional peak at lower frequencies, suggesting the presence of another gravity wave mode at the tower location. As will be discussed following Fig. 8, the tower location in the simulation does not show the most structured waves. The signal of the observed waves ($f = 0.017$ Hz and $\lambda = 350$ m) is much stronger at nearby locations.

Finally, all model spectra in Fig. 7 fall to zero at around 0.05 Hz. The missing high-frequency fluctuations are likely due to the effects of numerical truncation errors, the explicit filtering operation, and computational mixing, which is applied to damp out numerical noise. Computational mixing also removes small-scale motions that are part of the resolved turbulent field in high-resolution LES (Michioka and Chow 2008). Belusic and Guttler (2010) showed that by minimizing computational mixing, the mesoscale model spectrum could be raised to the observed magnitude, reproducing meandering motions during CASES-99. On the 25-m grid, fourth-order computational mixing is applied in the horizontal and vertical directions with a coefficient of $0.01\,\mathrm{s}^{-1}$. A smaller value of $0.005\,\mathrm{s}^{-1}$ results in numerical noise (i.e., $2\Delta x$ waves) in the flow field (not shown).

c. Sensitivity to nest domain

Model sensitivity to the placement of the nest domain is explored on the 25-m grid. The general rules of thumb for placing lateral boundaries in nested simulations (Zhong and Chow 2012) are 1) to extend as far away from the region of interest as possible (i.e., large domains), so that flows coming from the coarse outer grid Δ_c have sufficient time/space to develop turbulent motion resolvable on the inner grid Δ_f and 2) to avoid drastic changes in terrain, such that the lateral boundaries are located over smooth terrain whenever possible (Warner et al. 1997). While the first rule is usually limited by the available computational resources, the second rule depends more on the judgment of the modeler and the particular topography at the site. Over the CASES-99 site, the terrain is relatively simple and flat (Fig. 3), so it was not initially expected that the results would be sensitive to the placement of the nest domain.

Two domain sizes are tested on the 25-m grid with the TKE-1.5 closure. The smaller domain (TKE-S) has 192 grid points in both x and y directions, which is set by following a 5-to-1 nesting ratio from the 128-m grid. The larger domain (TKE) has 360 grid points. With identical model configurations, both the TKE-S and TKE runs produce a laminar-flow state for most of the night, but the TKE-S domain then transitions into a somewhat turbulent flow from 0500 to 0600 UTC (Fig. 6f), while the larger domain run fails to do so (Fig. 6b). The poorer model performance with increasing domain size is surprising. However, it is found that a shallow valley (Fig. 3) south of the main tower is an important topographic feature that strongly affects the flow. We attempt to address this counterintuitive result after exploring the role of the valley in the following section.

5. Turbulent bursting event

In this section, model results from the 25-m domain (DWL–ADM0) are used to reconstruct a 3D history of the formation, evolution, and breaking of the observed turbulent bursting event.

a. Source location

A north–south vertical slice of θ at 0531 UTC along line NS1 (Fig. 3) is presented in Fig. 8a. In the absence of
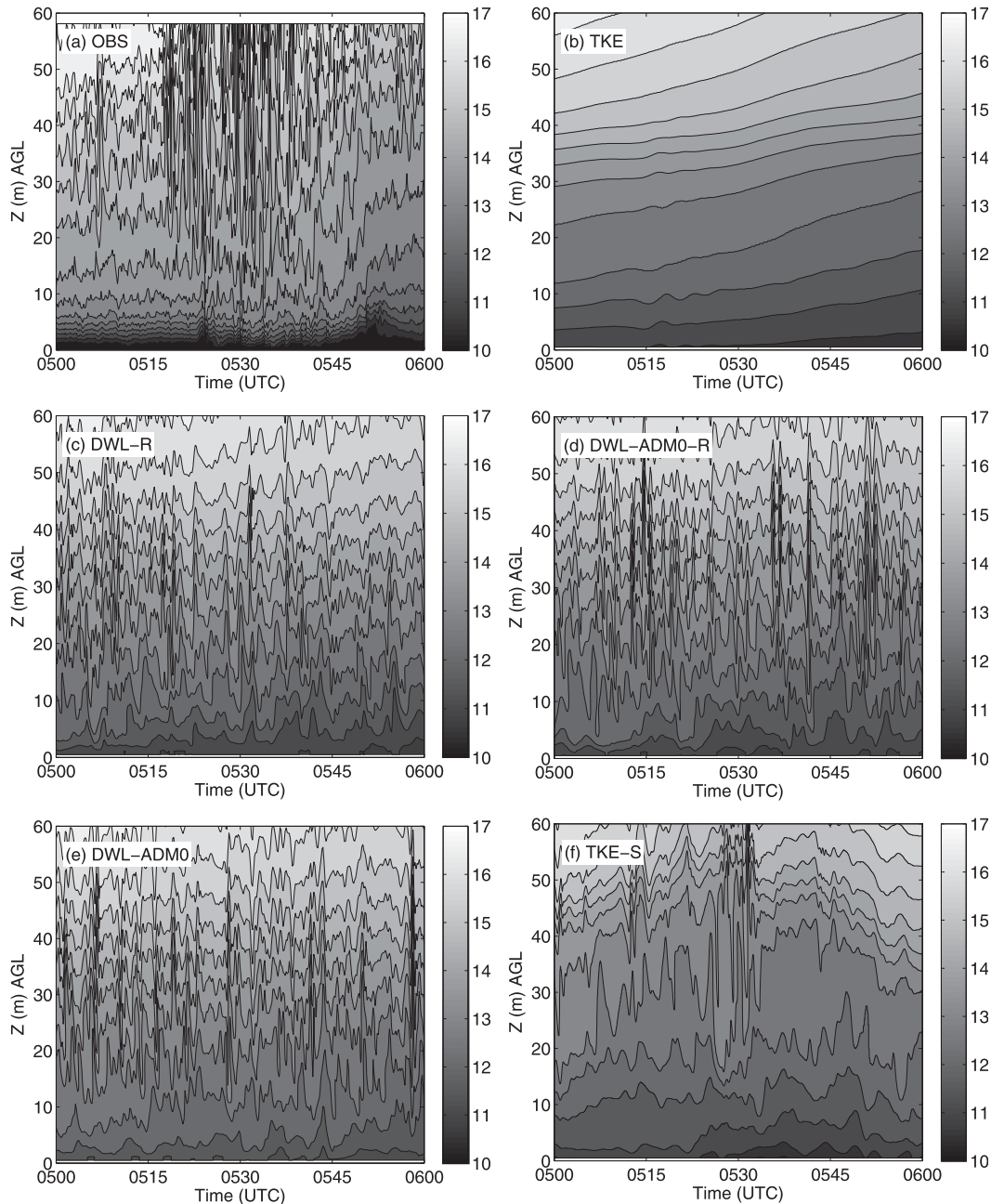
FIG. 6. Time–height contours of temperature from (a) thermocouple measurements and LES on the 25-m grid from the (b) TKE, (c) DWL-R, (d) DWL–ADM0-R, (e) DWL–ADM0, and (f) TKE-S runs. Contour interval is 0.5°C.

diabatic effects, isentropes of θ can be viewed as instantaneous streamlines, which the flow tends to follow (Cramer 1972). Wavelike motions are present in the region of the HRDL scan (enclosed between dashed lines), both in the simulations and in the observations (see Fig. 1). The waves are centered near 40 m AGL with respect to the tower site, and have horizontal wavelength $\lambda \approx 350$ m, agreeing with HRDL observations [see Fig. 2 and section 4c(3) in NB03]. A vertical slice of

θ in Fig. 8b (line NS2) at about 2 km east of the HRDL reveals the most organized waves with larger amplitudes. Figure 8c is as in Fig. 8b, except that it is from the 128-m run, and will be discussed in section 6.

Figure 8a indicates that the waves extend beyond the HRDL scanning range on both ends. As most clearly observed in Fig. 8b, a train of waves originates from the northern end of the valley and propagates toward the north. Moving downwind of the valley, waves grow and
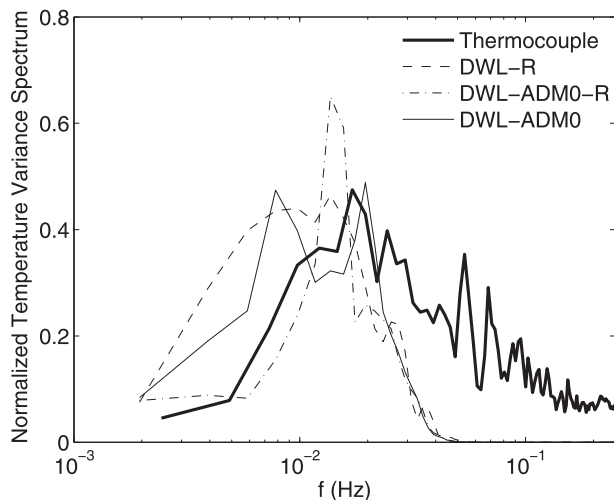
FIG. 7. Observed and simulated normalized temperature variance spectra during 0515–0542 UTC. Spectra are averaged with data between 30 and 60 m AGL and normalized by their respective temperature variance. LES data are recorded at 0.5 Hz and the thermocouple is recorded at 5 Hz.

steepen, reaching a maximum amplitude past $Y \approx 0$ km; they are finally damped in the far wake. In support of the valley origin of the waves, the isosurface of θ at 290.5 K is shown in Fig. 9. The isosurface dips over the upwind side of the valley, indicating descending motion into the valley. On the downwind side, the isosurface rises and exhibits coherent wave structures. Further downwind, the organized waves transition into a turbulent wake.

Having located the source of the waves in the upstream valley, we examine the valley cross section along line NS3 to investigate the space–time history leading up to the breaking waves. NS3 is chosen not only because the most intense wave motions are observed around this particular valley section (see Fig. 9), but more importantly for its relative topographic simplicity, as there are no major tributaries or gullies upstream of the main valley (Fig. 3). We first investigate a similar small-scale event around 0200 UTC along NS3, for its relative "cleanness" to demonstrate a plausible mechanism of wave breaking. At the end of this section, we show that the observed turbulent bursting event around 0530 UTC is of the same nature, and that the SBL goes through several cycles of evolving and breaking shear-instability waves governed by the same mechanism. In the following analysis, we also make use of three locations across line NS3 to represent the upwind location (UL), the valley location (VL), and the downwind location (DL) (see Fig. 3). Note that the valley location, where the strongest along-valley flow occurs, is slightly north of the valley bottom. This downwind shift is caused by the descending southerly synoptic flow.

Time series at four selected elevations at VL are presented in Fig. 10. Starting from [0000 UTC (1700 LST)], the SBL evolves in a classic fashion: winds accelerate under the synoptic forcing, while temperature decreases, first near the surface then extending upward. However, past 0110 UTC, U at 30 m AGL stops increasing and slips into a gradual decrease. This is followed by 70-m-AGL winds at 0130 UTC. The result is a vertical layer of near-constant wind speed between 30 and 80 m AGL from 0140 to 0200 UTC, during which a similar constant-θ layer is also observed. The anomaly is more clearly reflected in the time–height contours of vertical shear $[S^2 = (\partial u/\partial z)^2 + (\partial v/\partial z)^2]$ and buoyancy $[N^2 = (g/\theta)(\partial \theta/\partial z)]$ in Fig. 11a. A shear/buoyancy layer grows from the surface, reaching approximately 80 m AGL. Between the elevated and the surface layer is a region of minimal shear and buoyancy. The elevated layer decreases rapidly past 0200 UTC. This is due to a turbulent mixing event triggered by shear-instability waves, as discussed below. We divide the history of this particular mixing event at 0200 UTC into three time periods: formation, evolution, and breaking.

Finally, note that because of the complex nature of the flow, we do not exclude other mechanisms that might explain the observed intermittency. For example, Sun et al. (2012) showed that when wind speed exceeds a certain threshold, bulk shear can generate turbulence. Since we do observe an increase in synoptic winds as presented in Fig. 5a, the bulk-shear-generation mechanism is also one explanation. Another possibility is the increase of local pressure associated with the valley cold-air pool (explained below). The local pressure can oppose the synoptic flow and slow down surface winds.

b. Phase I formation

The history begins with the formation of a shallow valley drainage flow during the evening transition, which is frequently observed at the CASES-99 site (Mahrt et al. 2001). In Fig. 10, the surface wind at the valley station shifts from the synoptic (180°) to the a combined down-valley and downslope (115°) direction at around 0030 UTC and remains so except for the short period during the turbulent burst at 0200 UTC. An overview of the valley drainage flow is presented in Fig. 12. The surface streamlines in Fig. 12a are aligned in the north–south synoptic direction at 0000 UTC. Shortly after, streamlines in the valley switch to the east–west direction, approximately following the orientation of the valley in Fig. 12b. In comparison, near-surface winds at the tower location are synoptically driven. The wind direction is about 40° to left of the synoptic wind owing to the Coriolis effect (the full vertical sounding is presented
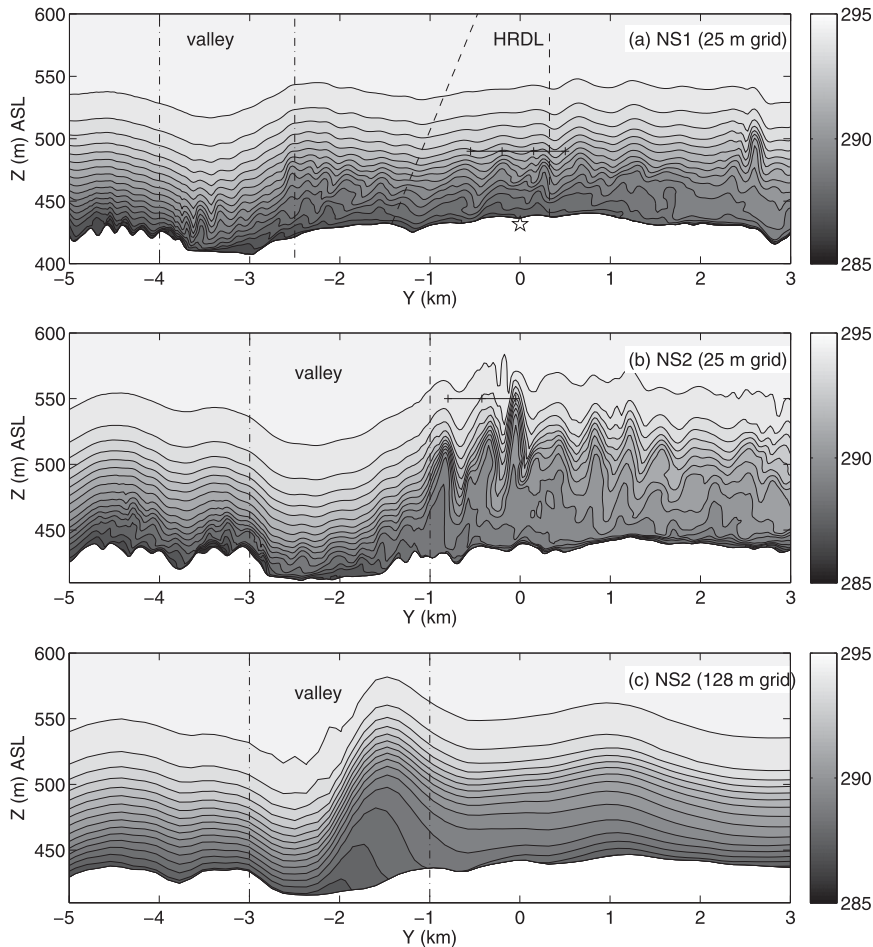
FIG. 8. Vertical cross sections of potential temperature on the 25-m grid along (a) line NS1, (b) line NS2, and (c) line NS2 at 0531 UTC on the 128-m grid. The HRDL scanning range is enclosed by dashed lines in (a). Approximate valley widths are enclosed by dashed–dotted lines. Solid horizontal lines separated by plus signs mark 350 m for each interval. Contour interval is 0.5 K.

in Fig. 4). The drainage flow advects cold air into the valley such that valley surface temperature drops nearly 7 K from 2300 to 0100 UTC; see Fig. 10. Mahrt et al. (2001) refers to this drainage flow associated cooling as "the early evening very stable period."

c. Phase II evolution

By the end of phase I, a very stable surface layer has established in valley. It can be viewed as a shallow cold-air pool that occupies the valley bottom. As the valley drainage flow continues, the cold-air pool deepens. Soon it is further supplemented by the downslope flows on both sides of the valley sidewalls. Figure 13 presents time series of the surface wind direction and temperature at the UL, VL, and DL locations (see Fig. 3). Past 0130 UTC, downslope flows at both the UL and DL locations carry colder air into the valley. Note that unlike

the UL side, the downslope flow on the DL side is nearly 180° opposing the synoptic wind.

The dimensionless parameter Nh/U (or inverse Froude number) largely determines the state of the stratified flow across valleys (Baines 1997). A critical value $|Nh/U|_c$ exists such that

$$\left|\frac{Nh}{U}\right| < \left|\frac{Nh}{U}\right|_c \quad \text{sweeping flow}$$

$$\left|\frac{Nh}{U}\right| > \left|\frac{Nh}{U}\right|_c \quad \text{stagnant valley fluid,} \qquad (7)$$

where h is the valley depth and N and U are buoyancy and velocity scales, respectively. Although the above criterion is derived based on constant N, we expect it to be applicable in bulk measures for nonconstant N in real situations. For hydrostatic flow over a Witch of Agnesi
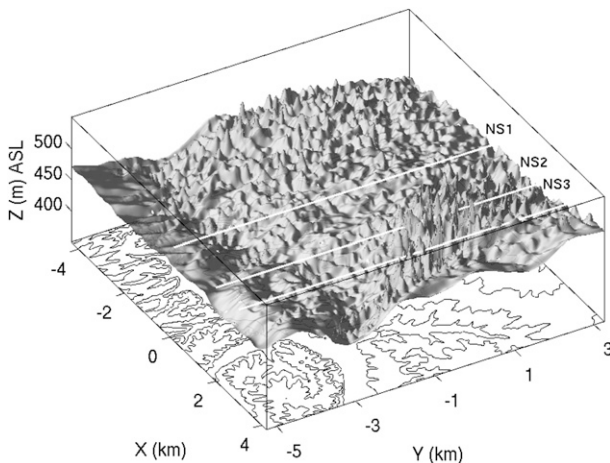
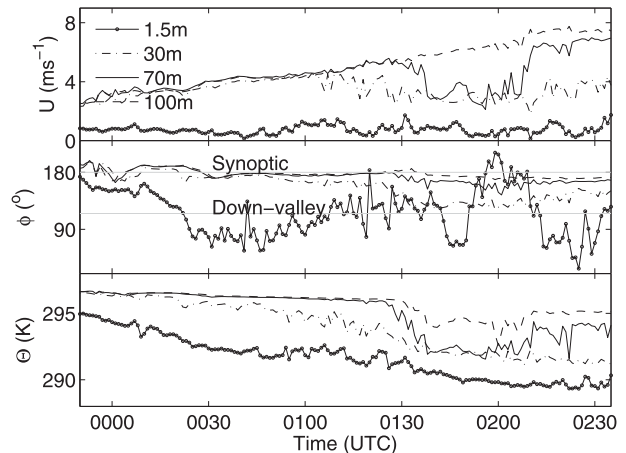FIG. 9. Isosurface height for potential temperature of 290.5 K at 0551 UTC. Data are from the 25-m grid.

FIG. 10. Time series of (top) wind speed, (middle) wind direction, and (bottom) potential temperature at four elevations at the VL location in Fig. 3. Data are from the 25-m grid.

valley, the critical value is 0.85 for uniform U and N (Miles and Huppert 1969). $|Nh/U|_c$ is unknown for the CASES-99 valley. However, given the shallowness of the valley ($h \sim 20\,\mathrm{m}$ deep) and the strength of synoptic winds ($U \sim 8\,\mathrm{m\,s^{-1}}$, measured at the top of the tower), we expect a small h/U. In other words, air within the valley is expected to be swept out by the cross flow. The strong stratification (high N) associated with the existing cold-air pool, however, shelters the valley fluid and lowers Nh/U, allowing antisynoptic downslope flows to form on the downwind side. The combined result is a stagnant cold-air pool inside the valley.

A standing gravity wave emerges downwind of the valley at 0100 UTC. Such waves are expected when the buoyancy time scale $2\pi/N$ is smaller than the advection time scale L/U across the valley, where L is the width valley ($\sim$1 km). This criterion can be expressed through another Froude number (Vosper and Brown 2008): $F_r = 2\pi U/NL \le 1$, where N and U are from the upwind flow. Figure 14 presents the vertical profiles of U and θ at the three locations at 0140 UTC, when a mature wave is observed (see Fig. 15). Taking the upwind U (5.4 m s^{-1}) at 40 m AGL as reference, where the profile is nearly uniform, and computing a bulk buoyancy frequency between 0 and 40 m AGL ($N \approx 0.06\,\mathrm{s^{-1}}$), we obtain $F_r \approx 0.57 < 1$. Similar standing waves are also observed above and downwind of a shallow valley of similar dimension in Vosper and Brown (2008).

The standing lee wave is somewhat nonclassic because it is injected with cold air from below. As the cold down-valley and downslope flows converge toward the downwind side of the valley, the comparatively warmer air in the valley bottom is forced to rise. In other words, the valley is continuously collecting cold surface flows and pushing relatively warmer air upward. By 0140 UTC, the standing wave evolves into a cold-air bubble, extending to nearly 70 m AGL, as shown in Fig. 15. Compared to the air under a standing wave, the upwind flow is warmer (see also Fig. 14). Therefore, it is forced to flow over the bubble and recovers downwind. The bubble essentially acts as a barrier that prevents horizontal transport of momentum from upwind.

Moreover, the cold-air bubble is capped by a strong inversion, developed mostly by compressing θ isotherms as it grows from below. The capping inversion suppresses turbulent mixing, which minimizes vertical transport of momentum from the fast synoptic flow above. Therefore, flow inside the bubble slows down compared to the upwind and downwind locations, as shown in Fig. 14. This effect is most clearly seen in vertical profiles at the VL location in Fig. 16. Three horizontal lines mark the approximate height of the capping inversion at three times during the evolution phase. It is remarkable that these lines also correspond to crossings in the velocity profiles, indicating slowing down of the flow once inside the inversion layer. From 0100 to 0125 UTC, the bubble grows from 16 to 50 m. Meanwhile, a decrease in wind speed is observed below 50 m, when flow accelerates above. Likewise, as the bubble grows from 50 to 76 m during 0125–0150 UTC, wind speed decreases below 76 m and it increases above. The same effect is also reflected in Fig. 10, as wind speed sequentially decreases at higher elevations.

d. Phase III shear-instability event

The capping inversion heights in Fig. 16 also correspond to inflection points in the velocity profiles. This is a result of reduced momentum over the depth of the bubble away from the surface. As the wind aloft
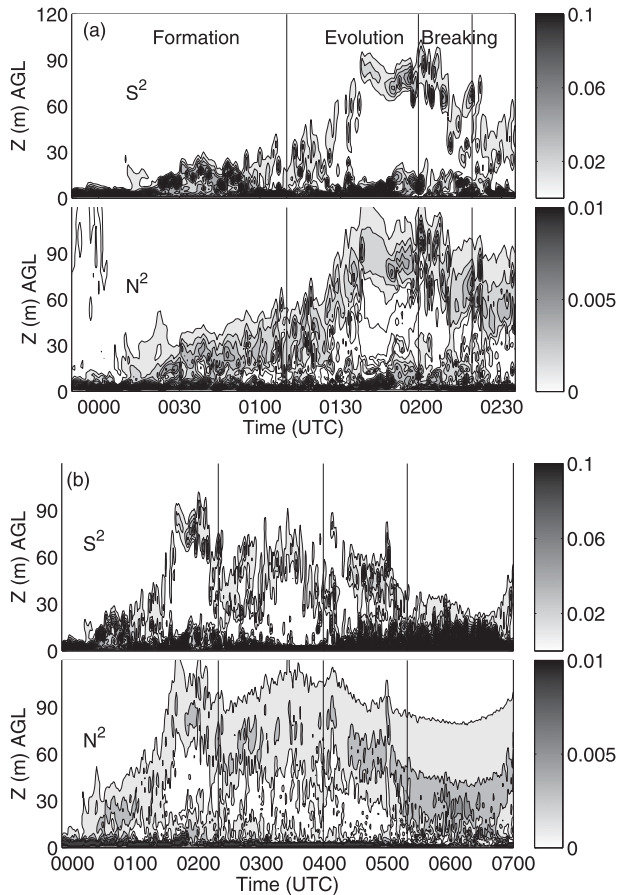
FIG. 11. Time–height contours of shear S^2 and buoyancy N^2 at the VL location (a) from 0000 to 0230 and (b) from 0000 to 0700 UTC. Contour intervals are $0.01\,\mathrm{s}^{-2}$ (S^2) and $0.001\,\mathrm{s}^{-2}$ (N^2). The vertical lines in (b) qualitatively separate out three cycles based on visual observations. Data are sampled every minute. Data are from the 25-m grid.
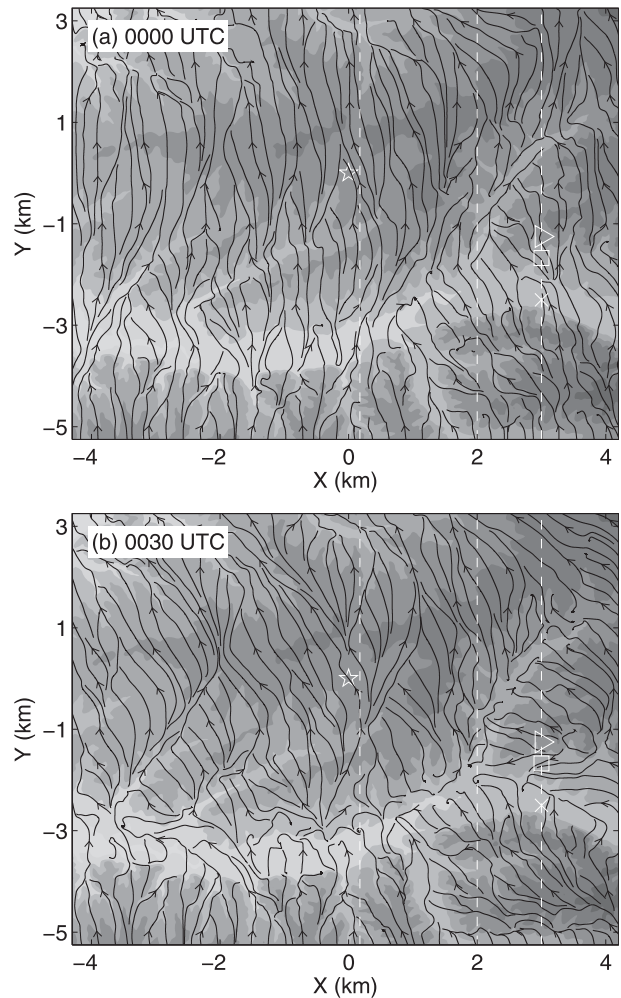

FIG. 12. Streamlines of surface wind at (a) 0000 and (b) 0030 UTC. Wind vectors are averaged over 5 min around the selected time. Data are from the 25-m grid. Shading denotes topography.

continues to accelerate under the geostrophic pressure gradient forcing (see 100-m wind speeds in Fig. 10), the increasingly inflected velocity profile eventually overcomes the stabilizing effect of buoyancy, and breaks into shear-instability waves. Figure 15 presents three snapshots of θ contours during the turbulent bursting event. At 0158 UTC, the standing wave sharpens on the downwind side, represented by the near vertical isentropes around $Y \approx -1.5\,\mathrm{km}$. In the next minute, waves with $\lambda \sim 275\,\mathrm{m}$ break from the lee side of the bubble and are advected downwind.

In linear instability theory, the initial linear instability from the inflection points is a Kelvin–Helmholtz wave (Drazin and Reid 2004). The wavelength is proportional to the spanwise vorticity thickness $\delta_\omega \equiv \Delta U/|dU/dz|_{\mathrm{max}}$, where ΔU is the difference between two free-stream velocities. The spanwise vorticity thickness is computed at 0150 UTC before the waves break. As shown in

Fig. 16, ΔU across the inflection point is estimated to be $5\,\mathrm{m\,s}^{-1}$, between 60 and 120 m where the wind speeds are fairly constant with height. The maximum elevated shear $|dU/dz|_{\mathrm{max}}$ is approximately $0.17\,\mathrm{s}^{-1}$. Therefore δ_ω, representative of the depth of the mixing layer, is approximately 30 m. The shear-instability wavelength is about 9 times larger than δ_ω. This value is larger than what linear stability predicts $\lambda \approx 7.8\delta_\omega$ (Michalke 1965), and much larger than DNS results $5.0\delta_\omega > \lambda > 3.5\delta_\omega$ (Rogers and Moser 1994). While inflection-point-induced shear instability is confirmed by the simulations, whether the observed waves are Kelvin–Helmholtz in nature is still questionable (R. Banta 2012, personal communication). This is because subsequent overturning of the KH billows downwind of the valley is hardly observed (see lidar scan in Fig. 1 and LES results in Fig. 8). Finally, we note that the inflection point can
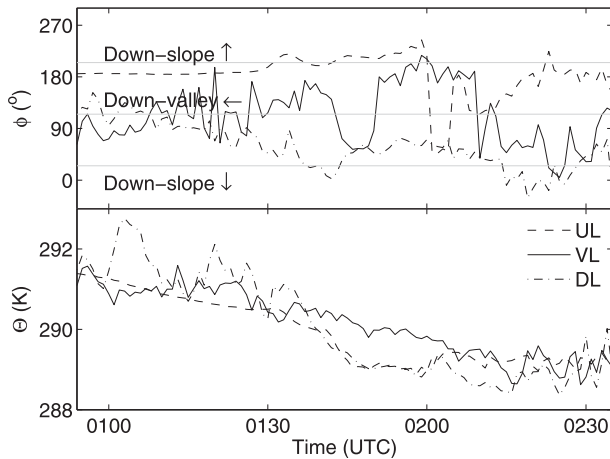
FIG. 13. Time series of (top) surface wind direction and (bottom) potential temperature at the three valley locations in Fig. 3. Arrows indicate approximate wind vectors. Data are from the 25-m grid.

also be removed by turbulence generated from the bulk wind (Sun et al. 2012).

When the standing wave sharpens and breaks on the downwind side, the cold air within is advected downwind. The absence of the cold air allows horizontal advection of warmer and faster upwind flow. The result is an increase in U and θ toward the upwind profiles, as shown in Fig. 17. However, the cold-air bubble is not completely swept out. The vertical extent of the replacement stops near 40 m AGL. Below, the flow stays more or less intact. Nevertheless, the shear-instability event also affects the surface flow. Surface winds at the valley location transition briefly into the synoptic direction in Fig. 10, and then back to the down-valley direction by 0230 UTC. Figure 17 shows the vertical extent of the direction shift to be about 8 m from the surface. This does not imply that the bursting event is felt at the surface. Rather, the wind shift is caused by the synoptic wind pushing the weaker cold-air bubble farther downwind.

e. Conceptual schematic

A conceptual schematic is presented in Fig. 18 to highlight the processes leading to shear-instability waves from the shallow valley. During evening transition, a valley drainage flow develops. It brings cold air into the valley, building up a shallow cold-air pool. In phase II, a standing wave forms on the downwind side of the valley based on the stratification, wind speed, and valley dimensions (i.e., the valley Froude number). In addition to the valley drainage flow, downslope winds develop on both valley sidewalls. The growing cold-air bubble inhibits both horizontal and vertical momentum and heat transfer. In phase III, the synoptic wind strengthens. Shear instability due to the velocity profile inflection at the top of the cold-air bubble leads to wave breaking.
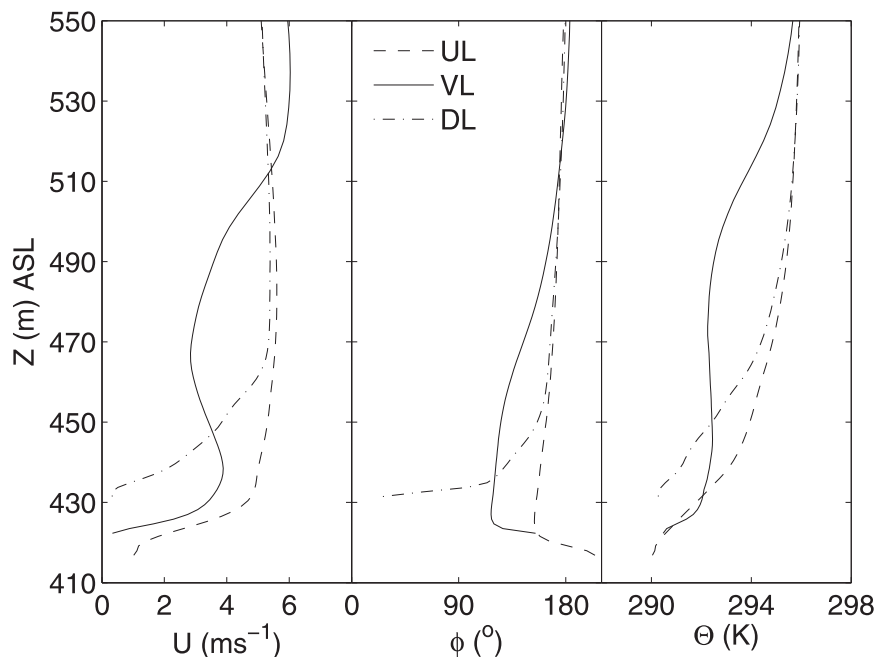

FIG. 14. Vertical profiles of (left) wind speed, (middle) wind direction, and (right) potential temperature at the three valley locations in Fig. 3 at 0140 UTC. Data are averaged over 5 min around the selected time. Data are from the 25-m grid.
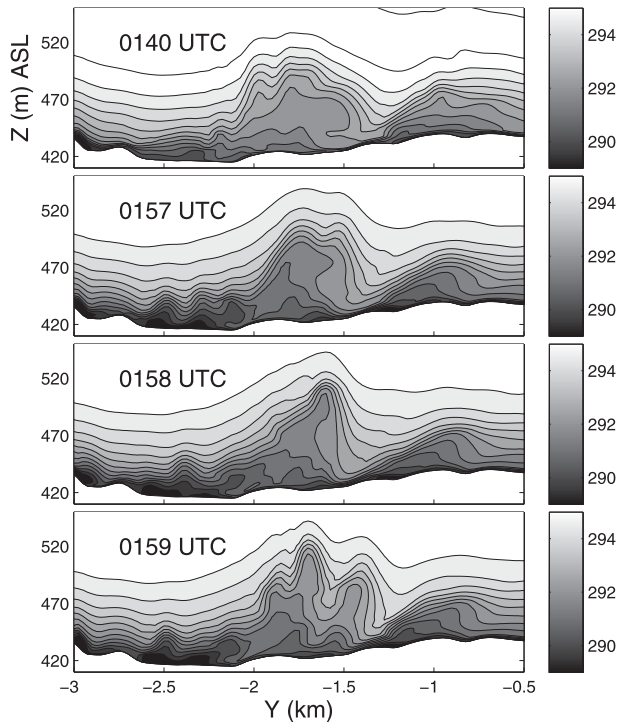
FIG. 15. Vertical cross section of potential temperature over the valley along line NS3 in Fig. 3 at 0140 and 0157–0159 UTC. Contour interval is 0.5 K. Data are from the 25-m grid.

Cold air is advected downwind and replaced by warmer air from upwind.

The process is cyclic in nature. It depends on the standing-wave formation across the valley as a result of strong stratification and also strong synoptic winds to generate enough shear to trigger turbulent mixing. After phase III, the downslope and down-valley flows are restored, and the cold-air bubble evolves again. Figure 11b presents an extension to Fig. 11a for the entire simulation. Three cycles are identified by visually tracking the elevated shear and inversion layer. The rising and strengthening of the elevated shear layer is a signature of the growing cold-air bubble, which is also associated with a decrease in wind speed from the top down and temperature from the bottom up. Wave breaking events are followed by falling and weakening of the elevated shear layer and an increase in U and θ. Although the signal is not as clear as during the first cycle, the third cycle corresponds to the observed event in NB03.

For the third cycle shown in Fig. 11b, the synoptic flow strengthens, and the standing wave (cold-air bubble) is pushed farther to the downwind side of the valley. It is expected that as Nh/U decreases, the dense fluid should be swept out of the valley. As shown in Fig. 8, the cold-air bubble is located on the downwind edge of the valley.

This results in a very energetic bursting event observed at the tower. However, it is not reflected properly in Fig. 11b, because the downwind side of the valley is no longer inside the cold-air bubble.

6. Terra incognita

In this section, we raise an important modeling issue for the SBL—namely, the terra incognita. The term was proposed by Wyngaard (2004), referring to the situation where the grid-resolution Δ is comparable to the dominant length scale l of the flow field. Taking convection, for example, the size of the largest eddy in the daytime convective boundary layer (CBL) spans roughly the boundary depth, $l \sim O(1\,\text{km})$. When running in mesoscale mode with $\Delta \sim O(10\,\text{km})$, convection cells are entirely SGS. This enables statistical treatments of the turbulent mixing processes in the CBL (i.e., the use of boundary layer parameterization schemes). On the other hand, in LES mode with $\Delta \sim O(100\,\text{m})$ or less, convective motions are explicitly resolved for the most part. The LES turbulence closure takes care of the remaining SGS motions. However, when Δ and l are of the same order, boundary layer parameterizations are no longer appropriate since the grid box is not large enough to contain a sufficient number of convection cells for statistical averaging. Meanwhile, l is too poorly resolved by Δ to be simulated with LES. Some techniques have been proposed for modeling in this gray zone, such as scale-aware parameterizations, and quasi-3D multiscale techniques (Arakawa et al. 2011), yet much remains to be developed.

While the terra incognita in the CBL is well recognized, the SBL counterpart has received little attention. This is because conventionally the dominant SBL length scale has been considered to be the buoyancy scale (e.g., the Ozmidov scale), which is approximately $O(10\,\text{m})$, and far beyond current high-resolution NWP (Beare 2011). However, if gravity waves are considered, the SBL terra incognita is already a pressing issue for practical applications. In the current study, the breaking shear-instability waves have $\lambda \sim 350\,\text{m}$, which are barely resolved on the 128-m grid. As a result, the standing wave persists throughout the night, as shown in Fig. 8c, compared to the 25-m grid results in Fig. 8b where the standing wave is eroded from the top through wave breaking owing to shear instability. This results in a colder, more stable, and less mixed boundary layer downwind the valley.

The question raised earlier in section 4c regarding why the small domain (TKE-S; see Table 3) is able to predict wave breaking, while the large domain (TKE) fails to do so, can be addressed in the light of the "terra
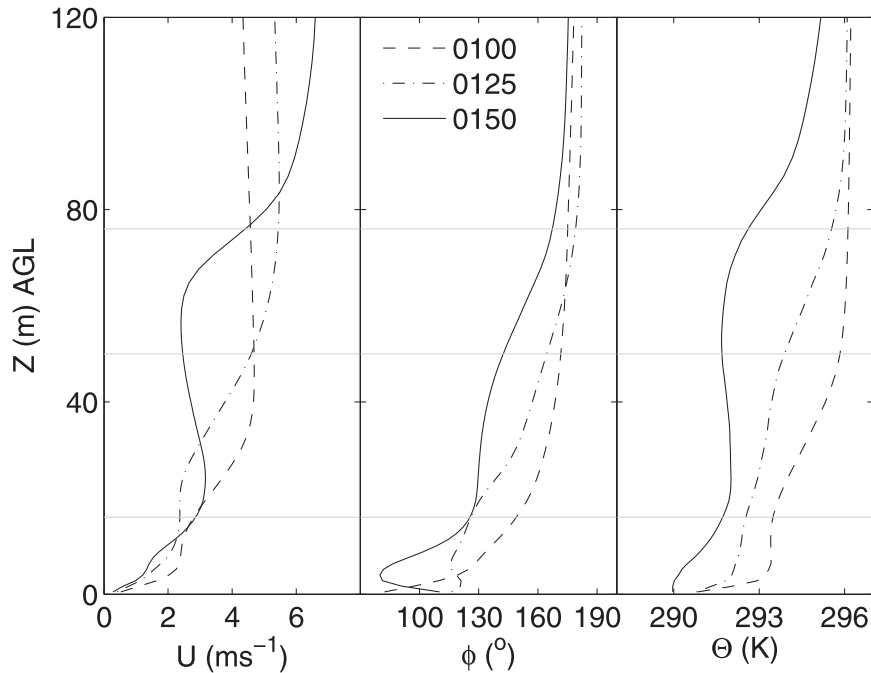
FIG. 16. Vertical profiles of (left) wind speed, (middle) wind direction, and (right) potential temperature at 0100, 0125, and 0150 UTC at the VL location in Fig. 3. Data are averaged over 5 min around the selected time. Data are from the 25-m grid.

incognita" as described above. The smaller LES domain is able to predict a semiturbulent flow, essentially because the southern boundary intersects the valley (Fig. 3). The standing wave from the 128-m grid is fed in as a boundary condition to the small LES domain. Because the 128-m grid is not able to predict wave breaking, the cold-air bubble is larger and stronger than it should be. The strength of cold-air bubble far exceeds the
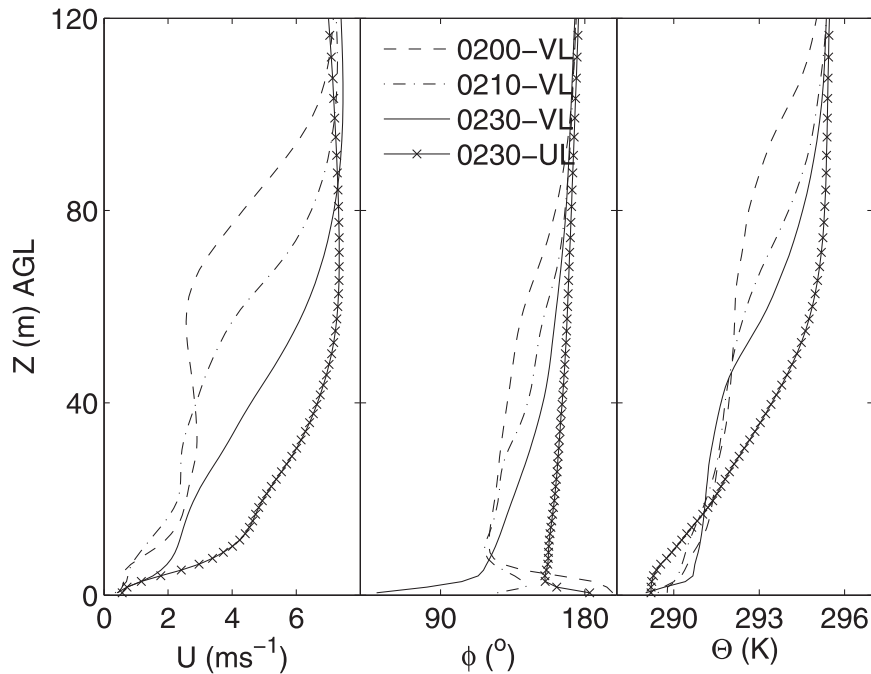

FIG. 17. As in Fig. 16, but for 0200, 0210, and 0230 UTC at the VL location, and for 0230 UTC at the UL location in Fig. 3.
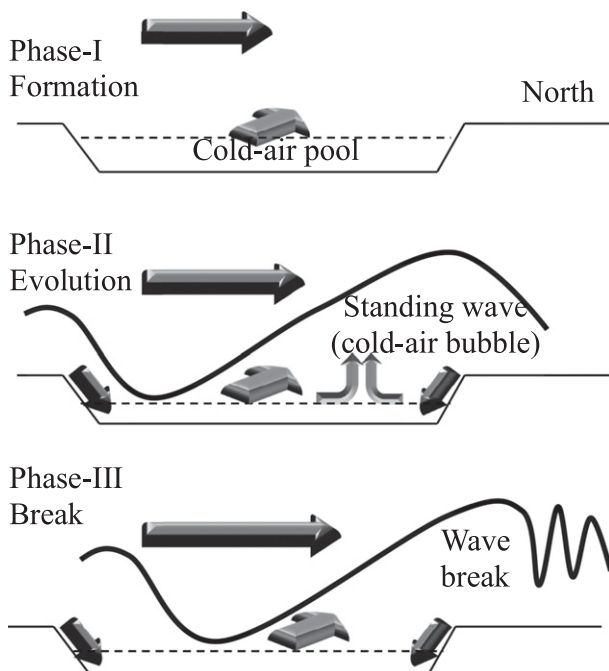
FIG. 18. Illustration of the shear-instability wave processes.

shear-instability criterion, such that the TKE-1.5 closure on the small domain (TKE-S) is able to predict the breaking event. In comparison, the standing wave is simulated locally on the large LES domain, which includes the entire valley. In this case, the TKE-1.5 closure failed to predict wave breaking primarily owing to its relatively dissipative nature, but the DWL–ADM0 closures captured this event well.

7. Summary and conclusions

High-resolution nested LES is performed to simulate an intermittently turbulent night (IOP2) during the CASES-99 field campaign. Simulations are performed over real terrain with realistic initial and lateral boundary conditions. The LES results are validated against surface and airborne observations. While the outer domains (640 and 128 m) capture the observed mean profiles, turbulent motions are only resolved on the 25-m LES grid. Furthermore, LES with the TKE-1.5 closure predicts a false laminar flow. Switching to a more sophisticated turbulence closure, the dynamic reconstruction model improves the model results and reproduces the observed turbulent bursting event. This demonstrates the usefulness of the DRM closure in sustaining SBL turbulence, while relaxing grid-resolution requirements (Zhou and Chow 2011). The improved representation of turbulence is achieved by adding resolved subfilter-scale (RSFS) stresses to the subgrid stress terms. It is shown

that the RSFS terms excite higher-frequency motions in the stratified flow, helping to sustain resolved turbulence. In this study, a zero-level reconstruction term improves the dynamic Wong and Lilly closure at minimal additional computational cost.

The high-resolution 3D flow field is then used to investigate the observed shear-instability wave event. The simulation reveals a plausible mechanism associated with breaking gravity waves. It is initiated from a standing wave formed across a shallow valley. The standing wave was preceded by the formation of a valley cold-air pool due to down-valley drainage flows. This evolved into a stagnant cold-air bubble fed by down-valley, downslope flows and was eroded by inflection-point-induced shear-instability waves. The cyclic process of formation and erosion was repeated during the night. This study answers the unresolved issue regarding the origin of shear-instability waves raised in NB03 and demonstrates the usefulness of LES to supplement field campaigns. Another lesson learned from the above intermittency mechanism is that when conducting nested SBL simulations over complex terrain, the modeler should be extra careful about grid placement even in seemingly flat topography. Under stratified conditions, even a shallow valley can have a significant impact on the SBL flow.

Finally, it is shown that besides the buoyancy length scale approximately $O(10\,\text{m})$, the terra incognita for the SBL should consider gravity waves approximately $O(100\,\text{m})$. In particular, it is shown that gravity wave breaking is absent when the wavelength is comparable to the grid spacing. Thus, if the terra incognita is unavoidable owing to computational constraints, suitable parameterizations should be developed to predict breaking gravity waves and represent the effects of induced turbulent mixing.

REFERENCES

Arakawa, A., J. H. Jung, and C. M. Wu, 2011: Toward unification of the multiscale modeling of the atmosphere. *Atmos. Chem. Phys.,* **11,** 3731–3742.

Baines, P. G., 1997: *Topographic Effects in Stratified Flows.* Cambridge University Press, 500 pp.

Bardina, J., J. H. Ferziger, and W. Reynolds, 1983: Improved turbulence models based on large eddy simulation of homgeneous, imcompressible, turbulent flows. Stanford University Tech. Rep. TF-19, 97 pp.

Beare, R. J., 2011: Modelling convective boundary layers in the terra-incognita. *Proc. Workshop on Diurnal cycles and the Stable Atmospheric Boundary Layer,* Reading, United Kingdom, ECMWF/GABLS, 83–90.

Belusic, D., and I. Guttler, 2010: Can mesoscale models reproduce meandering motions? *Quart. J. Roy. Meteor. Soc.,* **136,** 553–565.

Blumen, W., R. M. Banta, S. P. Burns, D. C. Fritts, R. Newsom, G. S. Poulos, and J. L. Sun, 2001: Turbulence statistics of a Kelvin–Helmholtz billow event observed in the night-time boundary layer during the Cooperative Atmosphere–Surface Exchange Study field program. *Dyn. Atmos. Oceans,* **34** (2–4), 189–204.

Carati, D., G. S. Winckelmans, and H. Jeanmart, 2001: On the modelling of the subgrid-scale and filtered-scale stress tensors in large-eddy simulation. *J. Fluid Mech.,* **441,** 119–138.

Chow, F. K., 2004: Subfilter-scale turbulence modeling for large-eddy simulation of the atmospheric boundary layer over complex terrain. Ph.D. dissertation, Stanford University, 339 pp.

——, and R. L. Street, 2009: Evaluation of turbulence closure models for large-eddy simulation over complex terrain: Flow over Askervein Hill. *J. Appl. Meteor. Climatol.,* **48,** 1050–1065.

——, ——, M. Xue, and J. H. Ferziger, 2005: Explicit filtering and reconstruction turbulence modeling for large-eddy simulation of neutral boundary layer flow. *J. Atmos. Sci.,* **62,** 2058–2077.

Cramer, O. P., 1972: Potential temperature analysis for mountainous terrain. *J. Appl. Meteor.,* **11,** 44–50.

Davies, H., 1983: Limitations of some common lateral boundary schemes used in regional NWP models. *Mon. Wea. Rev.,* **111,** 1002–1012.

Derbyshire, S. H., 1999: Boundary-layer decoupling over cold surfaces as a physical boundary-instability. *Bound.-Layer Meteor.,* **90,** 297–325.

Drazin, P. G., and W. H. Reid, 2004: *Hydrodynamic Stability.* 2nd ed. Cambridge University Press, 628 pp.

Gullbrand, J., 2001: Explicit filtering and subgrid-scale models in turbulent channel flow. Annual research briefs 2001, Center for Turbulence Research, 31–42.

——, and F. K. Chow, 2003: The effect of numerical errors and turbulence models in large-eddy simulations of channel flow, with and without explicit filtering. *J. Fluid Mech.,* **495,** 323–341.

Klemp, J. B., and R. B. Wilhelmson, 1978: The simulation of three-dimensional convective storm dynamics. *J. Atmos. Sci.,* **35,** 1070–1096.

Lund, T. S., 1997: On the use of discrete filters for large eddy simulation. Annual research briefs 1997, Center for Turbulence Research, 83–95.

Lundquist, J. K., 2000: The evening transition of the atmospheric boundary layer: Inertial oscillations and boundary-layer dynamics. Ph.D. dissertation, University of Colorado at Boulder, 160 pp.

Mahrt, L., D. Vickers, R. Nakamura, M. R. Soler, J. Sun, S. P. Burns, and D. H. Lenschow, 2001: Shallow drainage flows. *Bound.-Layer Meteor.,* **101,** 243–260.

Michalke, A., 1965: On spatially growing disturbances in an inviscid shear layer. *J. Fluid Mech.,* **23,** 521–544.

Michioka, T., and F. K. Chow, 2008: High-resolution large-eddy simulations of scalar transport in atmospheric boundary layer flow over complex terrain. *J. Appl. Meteor. Climatol.,* **47,** 3150–3169.

Miles, J. W., and H. E. Huppert, 1969: Lee waves in a stratified flow. Part 4. Perturbation approximations. *J. Fluid Mech.,* **35,** 497–525.

Moeng, C. H., 1984: A large-eddy-simulation model for the study of planetary boundary-layer turbulence. *J. Atmos. Sci.,* **41,** 2052–2062.

Nakamura, R., and L. Mahrt, 2005: A study of intermittent turbulence with CASES-99 tower measurements. *Bound.-Layer Meteor.,* **114,** 367–387.

Newsom, R. K., and R. M. Banta, 2003: Shear-flow instability in the stable nocturnal boundary layer as observed by Doppler lidar during CASES-99. *J. Atmos. Sci.,* **60,** 16–33.

Noilhan, J., and S. Planton, 1989: A simple parameterization of land surface processes for meteorological models. *Mon. Wea. Rev.,* **117,** 536–549.

Poulos, G. S., and Coauthors, 2002: CASES-99: A comprehensive investigation of the stable nocturnal boundary layer. *Bull. Amer. Meteor. Soc.,* **83,** 555–581.

Rogers, M. M., and R. D. Moser, 1994: Direct simulation of a self-similar turbulent mixing layer. *Phys. Fluids,* **6,** 903–923.

Steeneveld, G. J., T. Mauritsen, E. I. F. de Bruijn, J. V.-G. de Arellano, G. Svensson, and A. M. Holtslag, 2008: Evaluation of limited-area models for the representation of the diurnal cycle and contrasting nights in CASES-99. *J. Appl. Meteor. Climatol.,* **47,** 869–887.

Stolz, S., N. A. Adams, and L. Kleiser, 2001: The approximate deconvolution model for large-eddy simulations of compressible flows and its application to shock-turbulent-boundary-layer interaction. *Phys. Fluids,* **13,** 2985–3001.

Stull, R. B., 1988: *An Introduction to Boundary Layer Meteorology.* Kluwer Academic Publishers, 670 pp.

Sun, J., L. Mahrt, R. M. Banta, and Y. L. Pichugina, 2012: Turbulence regimes and turbulence intermittency in the stable boundary layer during CASES-99. *J. Atmos. Sci.,* **69,** 338–351.

Sun, W.-Y., and C.-Z. Chang, 1986: Diffusion model for a convective layer. Part I: Numerical simulation of convective boundary layer. *J. Climate Appl. Meteor.,* **25,** 1445–1453.

van Cittert, P., 1931: Der spaltbreite auf die intensitasverteilung in spektrallinien ii. *Z. Phys.,* **69,** 298–308.

Van de Wiel, B. J. H., A. F. Moene, O. K. Hartogensis, H. R. De Bruin, and A. M. Holtslag, 2003: Intermittent turbulence in the stable boundary layer over land. Part III: A classification for observations during CASES-99. *J. Atmos. Sci.,* **60,** 2509–2522.

Van Ulden, A. P., and A. A. M. Holtslag, 1985: Estimation of atmospheric boundary layer parameters for diffusion applications. *J. Climate Appl. Meteor.,* **24,** 1196–1207.

Vosper, S. B., and A. R. Brown, 2008: Numerical simulations of sheltering in valleys: The formation of nighttime cold-air pools. *Bound.-Layer Meteor.,* **127,** 429–448.

Warner, T. T., R. A. Peterson, and R. E. Treadon, 1997: A tutorial on lateral boundary conditions as a basic and potentially serious limitation to regional numerical weather prediction. *Bull. Amer. Meteor. Soc.,* **78,** 2599–2617.

Welch, P., 1967: The use of fast Fourier transform for the estimation of power spectra: A method based on time averaging over short, modified periodograms. *IEEE Trans. Audio Electroacoust.,* **15** (2), 70–73.

Winckelmans, G. S., A. A. Wray, O. V. Vasilyev, and H. Jeanmart, 2001: Explicit-filtering large-eddy simulation using the tensor-diffusivity model supplemented by a dynamic Smagorinsky term. *Phys. Fluids,* **13,** 1385–1403.

Wong, V. C., and D. K. Lilly, 1994: A comparison of two dynamic subgrid closure methods for turbulent thermal convection. *Phys. Fluids,* **6,** 1016–1023.

Wyngaard, J. C., 2004: Toward numerical modeling in the "terra incognita." *J. Atmos. Sci.,* **61,** 1816–1826.

Xue, M., J. Zong, and K. K. Droegemeier, 1996: Parameterization of PBL turbulence in a multi-scale nonhydrostatic model. Preprints, *11th Conf. on Numerical Weather Prediction,* Norfolk, VA, Amer. Meteor. Soc., 363–365.

——, K. K. Droegemeier, and V. Wong, 2000: The Advanced Regional Prediction System (ARPS)—A multi-scale nonhydrostatic atmospheric simulation and prediction model. Part I: Model dynamics and verification. *Meteor. Atmos. Phys.,* **75,** 161–193.

——, and Coauthors, 2001: The Advanced Regional Prediction System (ARPS)—A multi-scale nonhydrostatic atmospheric simulation and prediction tool. Part II: Model physics and applications. *Meteor. Atmos. Phys.,* **76,** 143–165.

Zang, Y., R. L. Street, and J. R. Koseff, 1993: A dynamic mixed subgrid-scale model and its application to turbulent recirculating flows. *Phys. Fluids,* **5A,** 3186–3196.

Zhong, S., and F. K. Chow, 2012: Mesoscale numerical modeling over complex terrain: Operational applications. *Mountain Meteorology: Bridging the Gap between Research and Forecasting,* F. K. Chow, S. F. J. De Wekker, and B. J. Snyder, Eds., Springer, 591–653.

Zhou, B., and F. K. Chow, 2011: Large-eddy simulation of the stable boundary layer with explicit filtering and reconstruction turbulence modeling. *J. Atmos. Sci.,* **68,** 2142–2155.